Coastal Engineering 42 (2001) 173–197
Coastal Engineering
An International Journal for Coastal, Harbour and Offshore Engineers
www.elsevier.com/locate/coastaleng

High-resolution field measurements and numerical modelling of intra-wave sediment suspension on plane beds under shoaling waves

K.P. Black [a,*], C.E. Vincent [b]

[a] Centre of Excellence in Coastal Oceanography and Marine Geology National Institute of Water and Atmospheric Research and Department of Earth Sciences, University of Waikato, PO Box 11-115, Hamilton, New Zealand
[b] School of Environmental Sciences, University of East Anglia, Norwich NR4 7TJ, UK

Received 9 April 1999; received in revised form 7 September 2000; accepted 27 September 2000

Abstract

Intra-wave sediment suspension is examined using high-resolution field measurements and numerical hydrodynamic and sediment models within 120 mm of a plane seabed under natural asymmetric waves. The detailed measurements of suspended sediment concentration (at 5 mm vertical resolution and at 4 Hz) showed two or three entrainment bursts around peak flow under the wave crest and another at flow reversal during the decelerating phase. At flow reversal, the mixing length was found to be approximately double the value attained at peak flow under the crest. To examine the cause of multiple suspension peaks and increased diffusion at flow reversal, a numerical "side-view" hydrodynamic model was developed to reproduce near-bed wave-induced orbital currents. Predicted currents at the bed and above the wave boundary layer were oppositely directed around flow reversal and this effect became more pronounced with increasing wave asymmetry. When the predicted orbital currents and an enhanced eddy diffusivity during periods of oppositely directed flows were applied in a Lagrangian numerical sediment transport model, unprecedented and extremely close predictions of the measured instantaneous concentrations were obtained. The numerical models were simplified to incorporate only the essential parameters and, by simulating at short time scales, empirical time-averaged parameterisations were not required. Key factors in the sediment model were fall velocities of the full grain size distribution, diffusion, separation of entrainment from settlement, and non-constant, but vertically uniform, eddy diffusivity. Over the plane bed, sediment convection by wave orbital vertical currents was found to have no significant influence on the results. © 2001 Elsevier Science B.V. All rights reserved.

Keywords: Intra-wave suspension; Numerical modelling; Field measurements; Waves

1. Introduction

Prediction of suspended sediment concentrations (SSC) at intra-wave time scales within a few centimetres of the seabed remains a challenge. The

* Corresponding author. Present address: ASR Ltd, PO Box 13048, Hamilton, New Zealand. Tel.: +64-7-856-9002; fax: +64-7-856-5036.
E-mail address: k.black@waikato.ac.nz (K.P. Black).

0378-3839/01/$ - see front matter
PII: S0378-3839(00)00058-2

timing of entrained concentrations through the wave cycle is not simply associated with peak crest and trough orbital currents, even over plane beds (e.g. Murray et al., 1991, 1993; Ribberink and Al-Salem, 1992). The concentrations vary through the wave cycle and with elevation above the bed. Laboratory measurements additionally indicate that suspension at flow reversal becomes more pronounced with increasing wave asymmetry, even though flow reversal suspension pulses are observed under symmetrical waves.

Murray et al. (1991, 1993) and Ribberink and Al-Salem (1992) measured at high vertical resolution in laboratory oscillating wave tunnels (which have rigid lids so "waves" have no vertical component) and found peaks in SSC under the wave crest, wave trough and around flow reversal. The laboratory measurements could be predicted numerically, if additional entrainment around flow reversal was included in the numerical model (Black, 1994). However, while concentration under the wave crest was proportional to instantaneous orbital current strength, flow reversal entrainment was an oddity, as currents were zero at the time. This is anomalous because SSC has been traditionally associated with bed shear stress and tractive force acting directly on the sediment grains (e.g. Bagnold, 1954; Vincent and Osborne, 1995).

Over rippled beds on a natural beach (Osborne et al., 1997), maximum concentration occurred around flow reversal when the orbital currents were decelerating (although no similar peak in concentration was evident during the accelerating phase). Over ripples, the bedform itself is associated with an upward ejection of sand by a vortex forming in the ripple trough. However, no similar explanation can be offered for the phenomenon over a plane bed when the timing of suspension must be intrinsic to the fluid dynamics, rather than an interaction between the fluid and the rhythmic bed-forming vortices (Savioli and Justesen, 1997).

It remains useful to study SSC numerically at short time scales in order to eliminate time and space averaging which can confound our understanding of the processes. Davies and Li (1997) have adopted numerical approaches to the problem and suggest that instability in the sheet flow layer in adverse pressure gradient conditions is potentially important for flow reversal peaks in suspension. However, they test a number of general model assumptions and systematically fail to reproduce either the phase or the magnitude of time-varying concentrations during the wave cycle. They also interpret the flow reversal SSC peak as being a "convection" event (i.e. vertical "bursting-type" currents transporting the sediment upwards) but the results of Black (1994) and the new data presented here do not fully support this interpretation.

In this paper, we present high-resolution acoustic field measurements of orbital velocity and SSC under shoaling waves, made within 30 cm of a plane bed (at 5 mm vertical resolution and 4 Hz). Moreover, we couple a Lagrangian sediment model with a high-resolution numerical hydrodynamic model to examine the relationship of SSC to boundary layer flow reversal.

There remains a need for systematic treatment of the micro-scale entrainment processes within 1 or 2 mm of the bed (Ribberink and Al-Salem, 1992; Flores and Sleath, 1998) but this matter is beyond the scope of the present paper and will be the subject of future work. We are also not treating bedload transport. In this paper, three main themes are addressed: (1) presentation and analysis of high-resolution field measurements of intra-wave SSC under shoaling waves; (2) mechanisms for flow reversal entrainment; and (3) developing accurate numerical predictions of hydrodynamics and intra-wave SSC while stripping the numerical models down to their fundamental essentials to expose the key processes and their simplest representation.

With the high-quality field data and process-based numerical simulations, there are no ad hoc parameter choices and vertical eddy diffusivity is obtained from model calibration. The modelling embodies relations for general use, including the Navier Stokes equations of momentum and conservation, a Lagrangian description of SSC, entrainment, multiple grain sizes, grain settlement, bed friction, non-linear advective momentum, surface pressure gradients, local acceleration, horizontal eddy viscosity, sea surface boundary conditions, near-bed reference concentrations, wave friction factors, gradient diffusion of SSC, wave orbital excursion formulae, bathymetry, water depth, initial conditions, sediment "pumping", washload, vertical convection and velocity shear.

The paper presents new field data that shows a number of interesting phenomena and so we are not aiming to simply compare modelling results with field data in order to "prove" the models. The modelling is based on existing methods but the application is new. Although it is the first time that such high-quality field data has been numerically simulated, a primary goal of the modelling is to identify the essential (fundamental) parameters needed to reproduce the field data in order to gain insight into sediment suspension. We prove the methodology by comparing the final model predictions to the measured suspended sediment concentrations.

While some of the results presented here could have been achieved with a simpler one-dimensional model, the side-view two-dimensional model has the additional capacity to treat horizontal advection of suspended sediment and can be generalised to irregular or rippled bathymetry (Black et al., 1997).

Wave asymmetry is shown here to play an important role in suspension by creating oppositely directed current shear near the bed around the time of flow reversal, predominantly during the decelerating phase (Savioli and Justesen, 1997). We are able to show that, with particular numerical procedures, very close predictions of the observed complex time series of instantaneous SSC can be achieved simultaneously at several vertical levels with pure gradient diffusion. Diffusion mechanisms have been questioned by Nielsen (1992); he dealt with larger-scale mixing (a few centimetres over flat beds) by imposing "convection" associated with small-scale vortices. We do not numerically treat these bursting-type suspension phenomena or small-scale vortices of the type considered by Nielsen (1992). However, our results provide weighty supportive arguments for the gradient diffusion assumption.

2. Field observations

Field measurements were carried out on Westshore Beach, Napier, New Zealand during November, 1997 (Fig. 1). The beach faces north-east and consists of well-sorted, medium sand with $D_{50} = 0.16$ mm (Table 1). The site was chosen because of its simple offshore bathymetry and the predominance of swell waves that must refract around an adjacent headland, causing the wave spectrum to narrow after the elimination of high frequency components in the offshore swell.

The experiments were conducted with the Sediment Micro-Probe which consists of a cantilevered frame supporting an Acoustic Doppler Velocimeter (Sontek ADV), a three-frequency Acoustic BackScatter sensor (ABS) and a micro-video (Fig. 2). The frame was carried out at low water to a location just beyond the breaker zone and connected by cable to a shore station.

One ABS transducer was directed to intersect the volume ensonified by the ADV. A second ABS transducer was mounted 0.60 m above the base of the frame, at the end of the cantilever, 0.45 m from the ADV and 0.75 m from the frame leg. The S4 current meter was placed at the other end of the cantilever, 0.25 m above the seabed. The concentrations measured by the ABS transducer close to the ADV were generally much higher than those from the ABS at the end of the cantilever and suspension events extended much higher into the flow: we believe that this was due to frame-induced suspension and so these data were rejected. The results from the ADV and the second ABS are reported here. Although the two instruments are separated by 0.45 m, waves were approaching normal to the instrument frame and the seabed was flat, and so there were no problems associated with phase lags or variations in bedforms. Over the plane bed, the ABS provided a clear reflection off the bed so that accurate vertical positioning of the measurements relative to the seabed could be achieved. Fig. 3 shows the burst-averaged concentration profile from the ABS; the break in slope at a range of 0.545 m from the transducer clearly defines the position of the seabed. The heights of the measurement "bins" quoted in this paper all have an uncertainty of ± 2.5 mm.

The video system consisted of a 600-mm optical glass fibre rod attached to a micro-video camera. A high-intensity light source was fed into the optical fibres and reflected light returned along the same route and into the camera. At the base of the optical rod, a mirror reflected the light at 90° so that the instrument looked sideways across the seabed, giving a better perspective. The field of view was about 15 mm across, allowing single sand grains to be

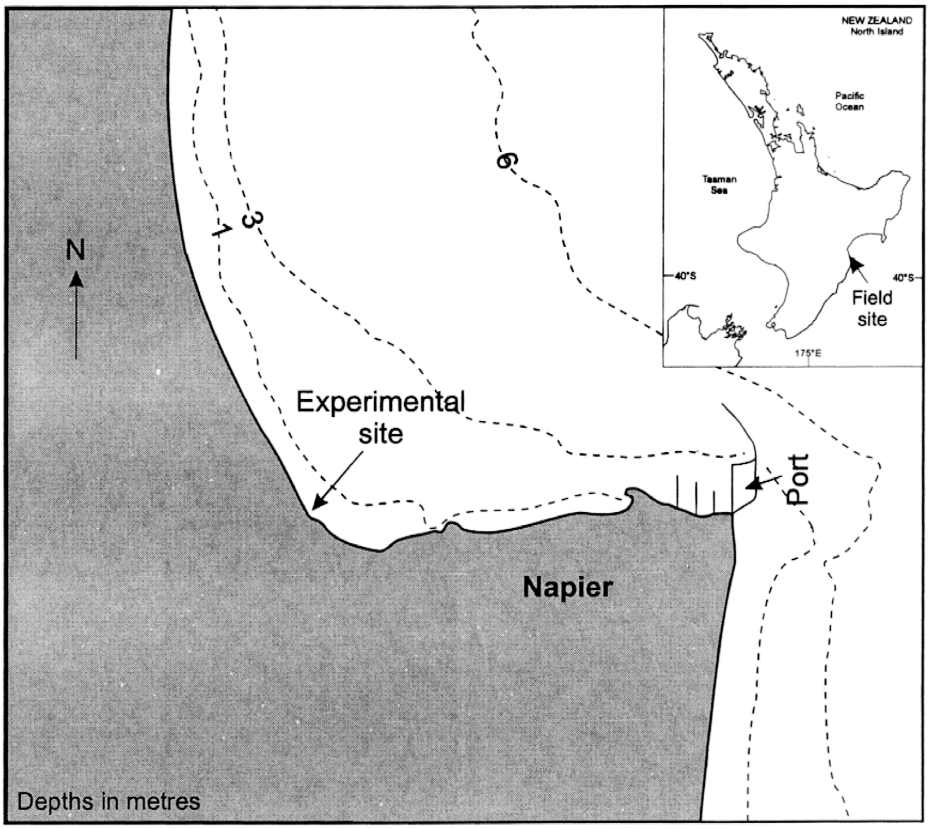

Fig. 1. Field site location at Westshore Beach, Napier, New Zealand. The wave direction during the experiments was from the southeast.

observed on the field-monitor and recorded for later analysis.

The camera, ADV and one of the ABS were suspended on a remotely controlled vertical profiling unit which consisted of a carriage raised and lowered by a stepper motor responding to commands from a portable computer at the shore (Fig. 2). The exact height of the staging above the bed was determined from the bed location reported by the ADV and by direct observations from the video. The high-resolution stepper motor allowed adjustments as small as 0.1 mm to be made.

Table 1
Grain size fractions used in the model simulation and percentage by weight

Fall velocity ($m\ s^{-1}$)	Grain size mm	Grain size φ	%
0.0360	0.2840	1.8162	10
0.0270	0.2313	2.1122	20
0.0200	0.1892	2.4022	40
0.0140	0.1511	2.7263	20
0.0100	0.1236	3.0157	10

The ABS and ADV were operated synchronously using a timing pulse to trigger a measurement every 0.25 s on each system. The ABS ensemble-averaged 12 profiles during each 0.25 s with a vertical resolution of 5 mm. Bursts of 1024 samples were taken with the ADV fixed at one height. Between bursts, the ADV was raised or lowered to obtain measurements in the potential flow or the wave boundary layer. The ABS was calibrated in a laboratory suspension tank using sand taken from the seabed close to the frame (Vincent and Downing, 1994).

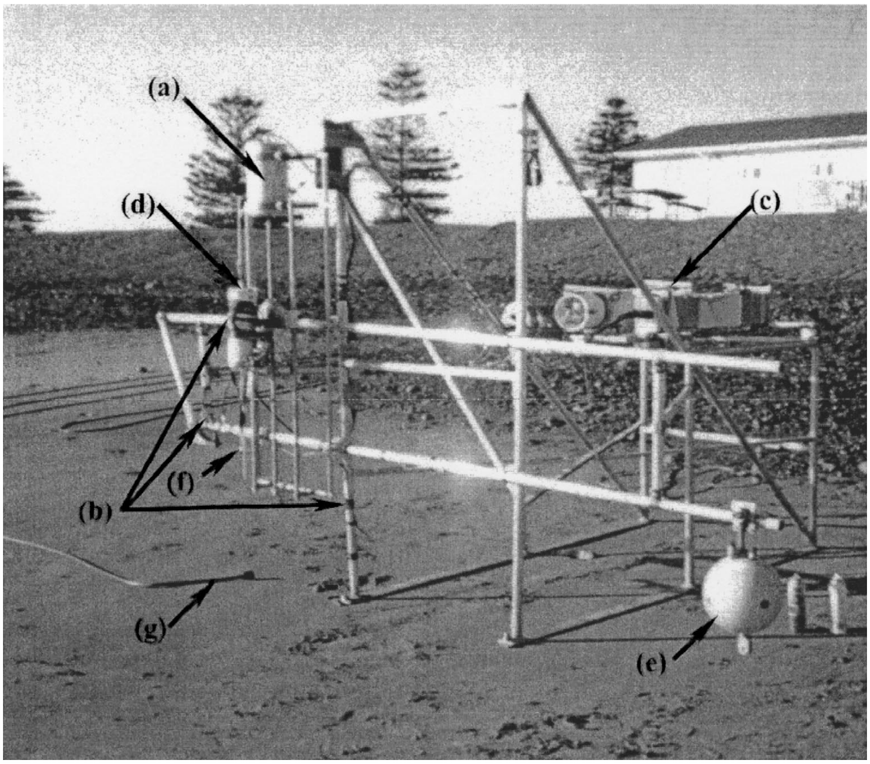

Fig. 2. Instrument frame. The instruments consist of: (a) Vertical Profiler Unit; (b) three Acoustic Backscatter Sensors; (c) instrument housings; (d) micro-video unit; (e) S4 electromagnetic current meter; (f) Acoustic Doppler Velocimeter; (g) umbilical cord to the shore.

A small systematic timing error (~ 1 s) was identified between the ADV and the ABS records. We expect the concentration very close to the seabed to be essentially in phase with the current close to the seabed. Thus, the two time series were aligned using the cross correlation between the ADV velocity and the concentration immediately above the seabed and a correction of 1.25 s was applied. The timing correction was opposite to that expected for phase changes due to friction as a flat bed is approached, i.e. the concentration led the velocity and this cannot be easily explained. The height of the ADV was varied from 6 mm to 0.23 m above the seabed during the experiments. No systematic change in the magnitude of the time lag with height was found and so we eliminate the possibility that the lag was associated with flow dynamics within the wave boundary layer. It was noted that the concentrations under the peak of the waves occurs nearly synchronously in the lowest 30 mm (six bins) suggesting that no significant phase lags exist between the concentration at 5 mm and the traction carpet at the seabed, as discussed below.

Results from two bursts (Runs 1 and 3) are examined in this paper. At this time, divers reported the bed to be flat under narrow-band swell with significant height $H_s = 0.42$ m and peak spectral period $T_p = 10.3$ s. The swell was approaching normal to the shore, while water depth was about 1.75 m and the break-point was 5–10 m shoreward of the frame. The longshore current during Runs 1 and 3 was small, approximately 0.01 m s^{-1} to the north (moving any frame-induced disturbance away from the ABS). Later as the tide rose, the seabed became rippled and a local sea developed on top of the swell (from the afternoon sea breeze), complicating the

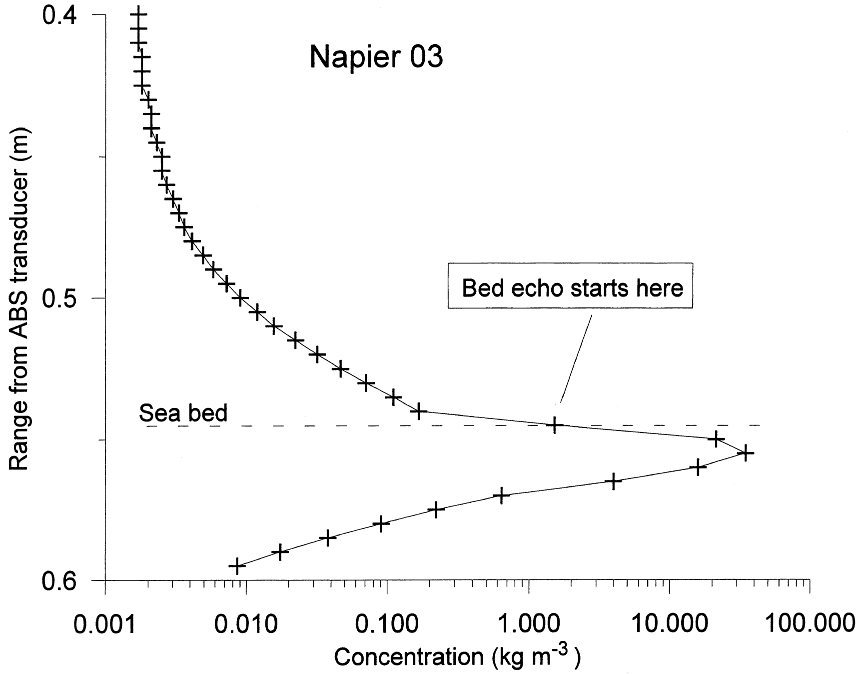

Fig. 3. Burst-averaged concentration profile for Napier Run 03.

wave field. During Runs 1 and 3, the ADV reported that the sampling volume was 6 and 7 mm above the seabed, respectively.

3. Field measurement results

When time-series averaged, suspended sediment concentration (SSC) for Run 3 varies smoothly with elevation (Fig. 3), but a transition occurs in the gradient of the profile at approximately 60-mm elevation. The near-bed reference concentration C_0, defined by extrapolation of a best-fit line (range vs. log(concentration)) through the six points immediately above the seabed is 0.242 kg m^{-3}.

The instantaneous SSC over the full duration of Run 3 exhibits a number of distinctive features (Fig. 4). SSC changes sharply over 3 orders of magnitude at 5 mm elevation while, at 120 mm, the SSC varies over a much smaller range and the magnitudes are approximately 1000 times smaller. With the arrival of a group of high waves, the lower levels respond immediately, such that SSC rises with the first wave in the group. SSC rises more slowly at 50 and 120 mm. At 130 and 240 s, the maximum SSC at 120 mm lags the lower levels by 20–30 s. Indeed, around 130 s, there is no evidence of waves 3 and 4 at 120 mm elevation; SSC only begins to rise between waves 4 and 5. Consequently, the upper level concentrations significantly lag the arrival of the wave group. A third characteristic of the time series is the slow decay of SSC after the passage of a wave group. For example, concentration at the lower levels takes approximately 30 s to decay after the large waves marked 3–7 have passed. On the contrary, the rise in concentration at the lowest levels is much more immediate, as depicted by the steeply rising leading face of the SSC time series.

The measured orbital velocities at 7 mm above the bed (Fig. 4) are characterised by a sharp crest and wider trough. Spectral analysis showed that the sharp-crestedness and the short-period secondary oscillations (prevalent behind the crest and in the trough) are associated with second and third harmonics of the peak wave frequency.

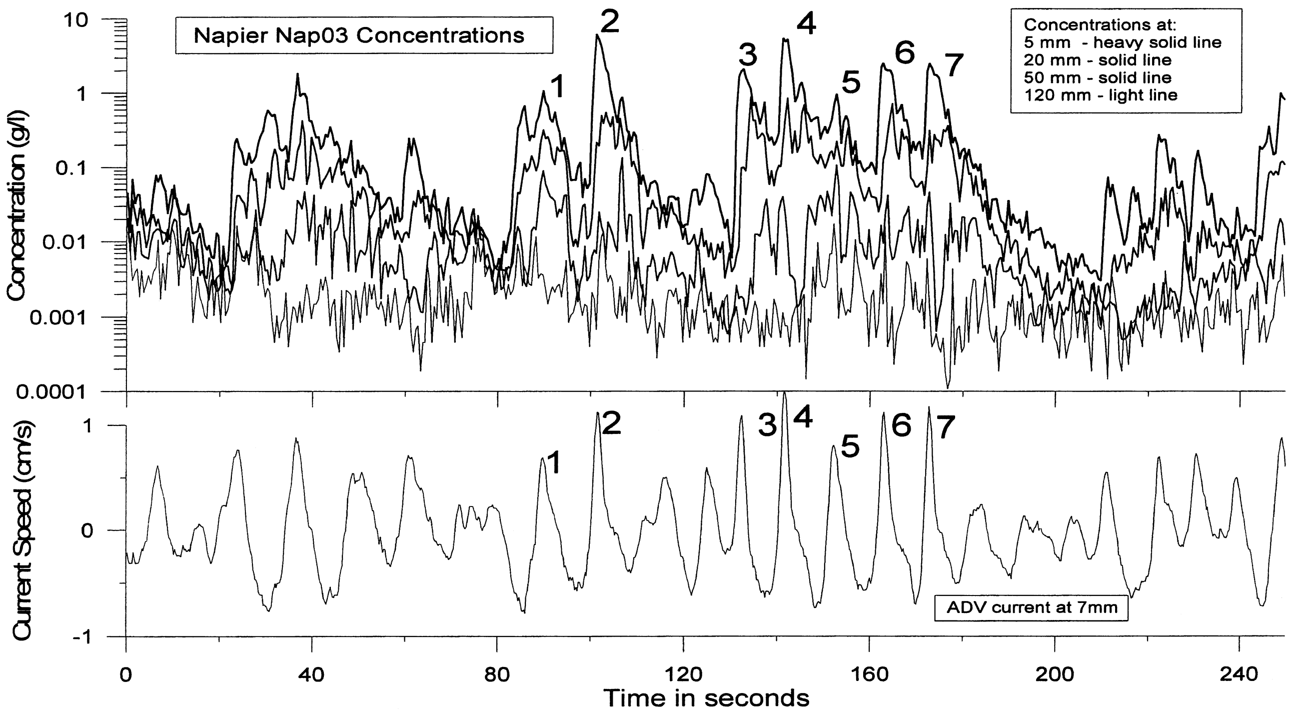

Fig. 4. Concentration profiles at four levels, 5, 20, 50 and 120 mm above the seabed and the shore-normal horizontal current speed from the ADV at 7 mm. The seven waves referred to later are also identified.

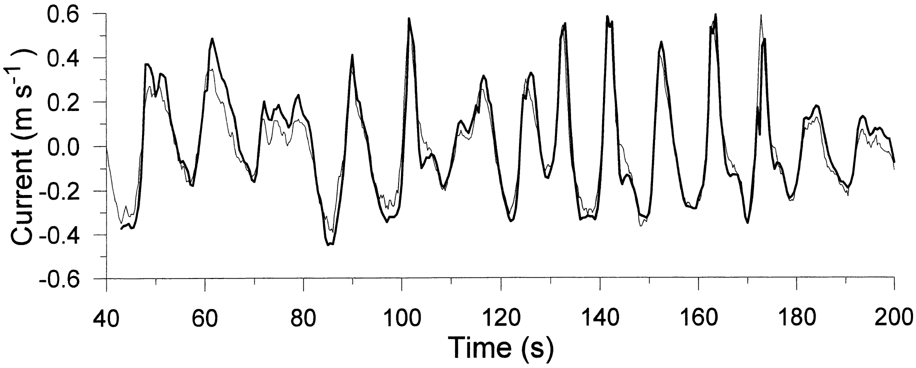

Fig. 5. A comparison of the velocity measurements from the S4 current meter at 250 mm (heavy line) and the ADV at 7 mm (light line).

The velocity profile often "broadens" after flow reversal on the trailing face (e.g. around 105 s). This tendency is not a boundary layer phenomenon because the orbital currents measured by the S4 at 0.25 m elevation are similar to the near-bed measurements (Fig. 5). Thus, the velocity patterns observed near the bed are primarily a consequence of surface wave motion, rather than a response restricted to the bottom boundary layer. However, there is a suggestion that the harmonic on the trailing face of several waves around flow reversal (e.g. at 105, 145 and 165 s) is less pronounced at 7 mm than at 0.25 m, and that the currents at the bed may lead the upper level flows at this time (Fig. 5). Currents are generally attenuated by seabed friction at the lower level.

The instantaneous SSC at 30-mm elevation appears to exhibit no relationship with orbital currents (Fig. 6). At 5 mm, highest concentrations occur

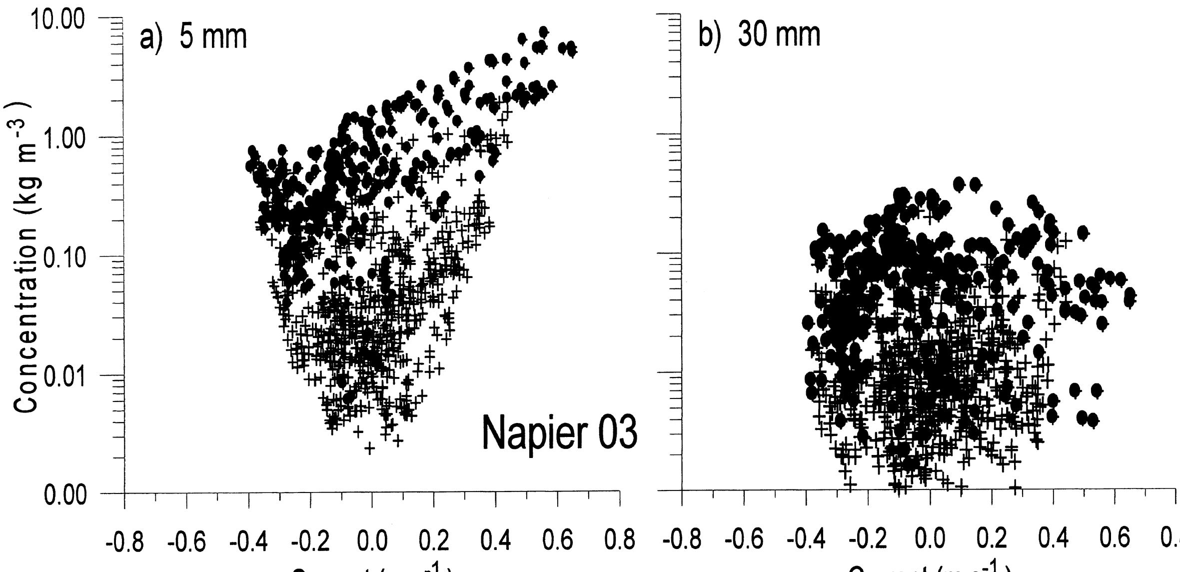

Fig. 6. Suspended concentrations at 5 mm (a) and 30 mm (b) above the seabed as a function of the current at 7 mm. The filled circles are from waves 1–7 (Fig. 4) and the crosses are from the rest of the burst.

mostly at peak flow under the crest as expected, but the relationship remains scattered. The clear asymmetry at 5 mm between the suspension under the crests (+ve) and that under the troughs is not apparent at 30 mm. Although instantaneous current speeds reach 0.3–0.4 m s^{-1} under the troughs of the wave groups, the suspension close to the seabed is systematically less than at similar speeds under the crests. Evidently, instantaneous SSC cannot be predicted from a simple empirical relationship with orbital currents, even when currents and SSC are both measured very close to the bed.

Fig. 7 shows in more detail the period from 120–190 s, covering waves 3–7, with concentration time series from the lowest six bins at 5–30 mm above the bed. Close to the seabed, the primary peak is in phase with the peak orbital currents, but other secondary peaks occur. The primary peak near the bed tends to be short and sharp, with concentrations rising and falling rapidly.

Further up the profile at 30 mm, the largest peak occurs after flow reversal rather than after the passage of the wave crest. For example, the maximum SSC under waves 3, 4 and 7 occurs after flow reversal at 30 mm even though at 5 and 10 mm elevation the main peak is associated with the wave crest. Thus, the relative importance of the "primary" and "secondary" peaks changes as distance increases from the seabed, with the secondary peak becoming dominant, typically by 20 mm from the bed, and the primary peak disappearing by 30 mm.

The secondary peak starts at, or soon after, flow reversal and lasts for 3–5 s. The concentrations are lower in this peak, but the concentration gradients are also much smaller, suggesting higher levels of turbulent mixing at this time. Examining Fig. 7 in

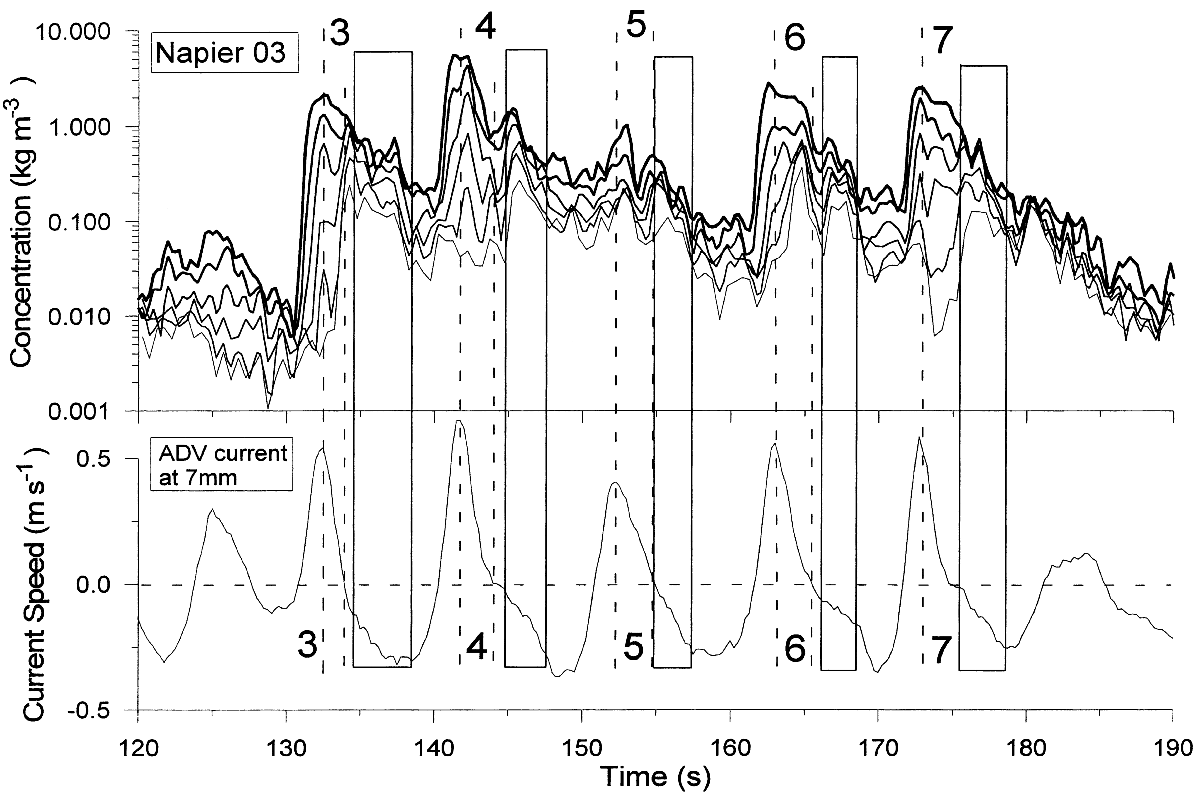

Fig. 7. Suspended sand concentrations at 5, 10, 15, 20, 25 and 30 mm above the seabed (upper) and current speed (lower) for the period 120–190 s. Vertical dotted lines show the times of peak current and decelerating flow reversal. The boxes indicate the periods when the sediment entrains around flow reversal.

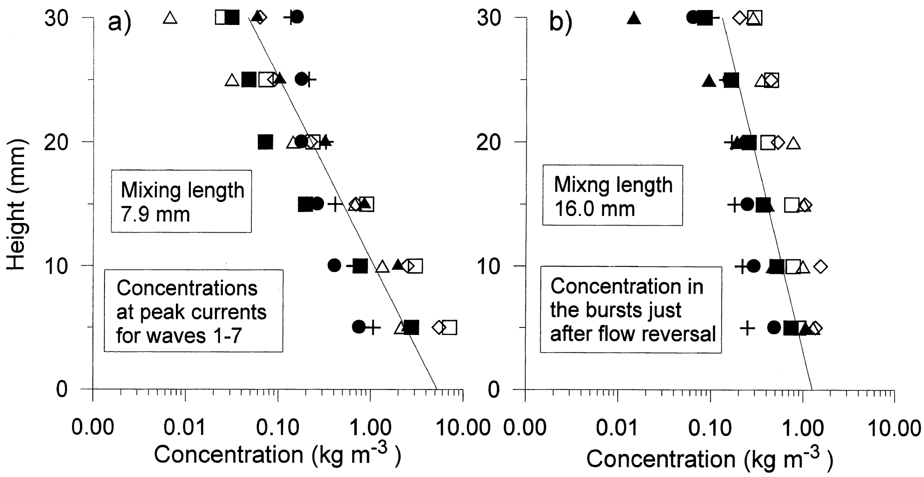

Fig. 8. Concentration profiles under (a) the peak current velocities and (b) at the start of each burst following flow reversal, at six heights for waves 1–7. The mixing lengths are derived from the average of the best-fit lines for each profile. The mixing length is defined in Eq. (8).

detail, the isoline spacing is variable, suggesting that eddy diffusivity varies during the wave cycle and from wave to wave.

Instantaneous vertical profiles of SSC were obtained by extracting concentrations from the time series at the times when concentration at the 5 mm level reached a local maximum. This was done for the seven waves, both at the wave crest and after flow reversal. When averaged over the seven waves, we obtained by linear regression a mixing length of 7.9 mm under the wave crests and 16 mm at flow reversal (Fig. 8). For a median fall velocity of 0.02 m s^{-1}, the corresponding eddy diffusivities (Eq. (7)) are 0.00016 and 0.00032 m^2 s^{-1} under the crest and around flow reversal, respectively. This factor of 2 increase in eddy diffusivity explains why highest concentration at 30 mm is associated with flow reversal rather than the wave crest.

One additional recurring characteristic of the time series is the twin peak in SSC associated with the wave crest. The twin peak is most pronounced for waves 3, 4 and 6, and is most evident at 10–20 mm.

4. Numerical modelling

The field measurements indicate that instantaneous SSC cannot be predicted from orbital motion alone, even when both are measured near the bed. Indeed, the high-resolution data clearly show that the relationship between these variables becomes almost totally scattered with elevation above about 20–30 mm. This suggests the need for a more comprehensive numerical approach. In the following sections, we use coupled hydrodynamic and sediment transport models. While the near-bed orbital currents were directly measured and could have been applied, we use a numerical hydrodynamic model for several reasons: (1) the model provides insight into near-bed dynamics and shear; (2) the shear in the boundary layer can be predicted and used for the sediment transport modelling; (3) the importance of vertical convection associated with wave orbital motion can be tested; (4) horizontal advection can be treated throughout the water column; and (5) the case study demonstrates our predictive capacity to simulate both the near-bed hydrodynamics and SSC.

4.1. Hydrodynamics

To model the wave orbital motion, the three-dimensional hydrodynamic and advection/dispersion model 3DD was adopted (Black, 1995). The model has been widely used for baroclinic and barotropic continental shelf and estuarine investigations (Black, 1995) and for micro-scale boundary layer simulations over bedforms (Black et al., 1997) but this paper presents the first micro-scale application over a plane seabed. We adopted 3DD's side-view capacity (a sub-set of the full three-dimensional model) to establish a grid of 60 horizontal cells and 28 vertical cells (layers). Horizontal cell dimensions were 100 mm, while the vertical grid size ranged from 100 mm near the surface to 10 mm in a series of cells at the bed. Of relevance to this paper, the model treats horizontal and vertical eddy viscosity, non-linear convective momentum, pressure gradients and bed frictional resistance.

The vertical eddy viscosity is taken as vertically uniform in both the hydrodynamic and sediment transport models. We have also assumed that eddy viscosity is equal to eddy diffusivity. These assumptions were tested by model calibration, comparing measured and predicted SSC.

The eddy diffusivity magnitudes were obtained by calibration of the sediment model which is very sensitive to the parameter. However, over the range of the eddy diffusivities being considered in this paper (later shown to be 0.00025 to 0.00050 m^2 s^{-1}), sensitivity tests revealed that the hydrodynamic model is not affected by the eddy viscosity magnitude. Fig. 9a shows the predicted currents at 15 mm above the bed for three different cases of vertical eddy diffusivity: (1) uniform at 0.00025 m^2 s^{-1}; (2) uniform at 0.00050 m^2 s^{-1}; and (3) obtained from a standard parabolic mixing length formula. The predictions for the three cases are indistinguishable (Fig. 9a).

The assumption of uniform vertical eddy viscosity and diffusivity may appear bold in the light of the many laboratory measurements that show a linear mixing length gradient with elevation near the bed, theoretically caused by a reduction in eddy size as the bed is approached. However, prior model studies, this paper and near-bed measurements of the authors over plane beds have consistently demonstrated that uniform eddy viscosity gives the best results near the bottom, say the lowest 100 mm. Possibly, the high

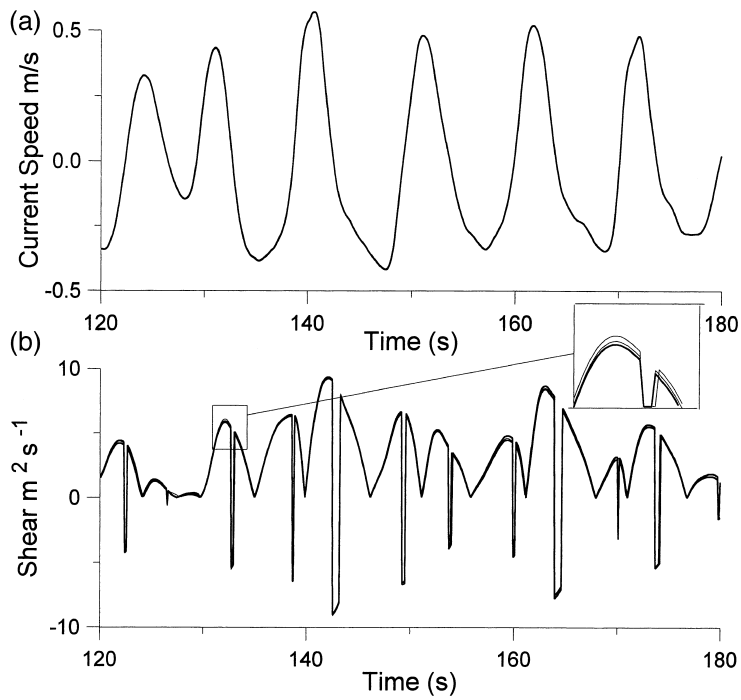

Fig. 9. (a, top panel) Comparison of velocities predicted by the numerical hydrodynamic model at 15 mm above the bed in three cases: (1) uniform vertical eddy viscosity of 0.00025 m^2 s^{-1}; (2) uniform vertical eddy viscosity of 0.00050 m^2 s^{-1}; and (3) with a standard parabolic mixing length formula of $l_s = Kz(1 - z/h)$, where $K = 0.4$, z is elevation and h is water depth. (b, bottom panel) Shear obtained from the numerical hydrodynamic model between levels at 5 and 25 mm above the bed for the same three cases in (a).

grain concentrations, fluidisation between the grains making the "bed level" less discernable, micro-scale irregularities and wave randomness disrupt the classic smooth-plate laboratory profiles. These factors may create a more evenly mixed region of uniform diffusivity near the bed in natural environments, rather than a linearly increasing mixing length with elevation. Most importantly, under a gradient diffusion assumption, it is essential to have non-zero diffusion at the bed, otherwise, grains simply cannot be lifted into suspension.

The boundary conditions for the velocity are no slip at the bed and zero shear stress at the surface. Seabed roughness length is taken as $z_0 = k_s/30$, where $k_s = 2.5D_{50}$. Water level boundary conditions were calculated using the measured instantaneous horizontal orbital currents $U(x,z,t)$. Assuming a linear shallow-water approximation:

$$\xi(t) = \xi_0 + U(x,z,t)\sqrt{h/g} \tag{1}$$

where $\xi(t)$ is the oscillating water level, ξ_0 is a mean water level offset, h is the average water depth in the grid (including the offset) and g is gravitational acceleration (9.81 m s^{-2}).

Over the short space scales being considered, the water levels were assumed to be unaltered by their passage across the 6-m-long grid. The time lag across the grid was calculated by integrating the bathymetry to find the mean shallow-water phase speed, which over a plane bed simply reduces to:

$$\bar{C} = \sqrt{gh}\,. \tag{2}$$

The time lag is then $T_L = d/\bar{C}$, where d is the distance across the grid between the open boundaries.

When used to obtain hydrodynamic model boundary conditions, the time series $U(x,z,t)$ (at $z = 6$ and 7 mm in Runs 1 and 2, respectively) included both wave orbital and turbulent components and so it was smoothed using a box-car window of 13 data points to eliminate the latter. The time series was then multiplied by a compensating factor of 1.6 and 1.5 for the segments above and below the mean, respectively to overcome the wave orbital amplitude attenuation caused by the filter. The two factors were obtained by separately considering the crest and trough of the wave, due to wave asymmetry. While more complex spectral smoothing and tapered windows were tested, it was found that the harmonics play an important role and so a spectral cut-off frequency that eliminated the turbulence only was not easily chosen.

4.2. Sediment dynamics

Sediment transport was modelled with POL3DD, a three-dimensional Lagrangian model (coupled to 3DD) which adopts the adaptations of previous micro-scale intra-wave modelling (e.g. Black, 1994; Black et al., 1995). The model treats advection, diffusion, entrainment and settlement of a population of grain sizes. Contrary to previous studies, velocities are taken from the numerical hydrodynamic model rather than from direct measurements of orbital currents.

The near-bed reference concentration associated with local sediment entrainment over plane beds is described by the Nielsen (1986) formula:

$$C_0 = 0.005\rho_s\theta^3 \tag{3}$$

where ρ_s is the sediment density and θ is the instantaneous skin friction Shields (1936) parameter given by:

$$\theta = \frac{f_w U_w^2}{2sgD} \tag{4}$$

in which f_w is the wave friction factor, U_w is the instantaneous wave orbital velocity, s is the relative density of the sediment ($s = (\rho_s - \rho)/\rho$) and ρ is the density of sea water. The grain size D is taken as the median size D_{50}.

Swart (1974) noted that f_w is a function of the ratio of a length scale r representative of the bed roughness to the semi-orbital excursion a, and found an empirical relationship:

$$f_w = \exp\left(5.213\left(\frac{r}{a}\right)^{0.194} - 5.977\right). \tag{5}$$

For flat beds, the roughness $r = 2.5D_{50}$ was adopted, while the orbital excursion (Black and Rosenberg, 1991) was:

$$a = U_{\mathrm{rms}} T_{\mathrm{p}} / 2\pi \tag{6}$$

where T_{p} is peak spectral period and U_{rms} is the root-mean-square orbital current. It is stressed here that the wave friction factor is used only for the sediment entrainment in Eqs. (3) and (4). This is justified by previous modelling (e.g. Black, 1994) and because the wave friction factor is applied in an empirical Eq. (3) that has coefficients which are dependent on the choice of friction factor formula. As such, it is necessary to follow the precedents to be compatible.

For a vertically uniform near-bed eddy diffusivity, l_{s} is a mixing length given by:

$$l_{\mathrm{s}} = E_{\mathrm{v}} / w \tag{7}$$

where E_{v} is the vertical eddy diffusivity and w the sediment fall velocity. The mixing length is defined in the equation for concentration at elevation z given by:

$$C = C_0 \exp(-z/l_{\mathrm{s}}) \tag{8}$$

where C_0 is given by Eq. (3).

Instantaneous currents used to calculate near-bed reference concentration throughout the model domain (Eqs. (1) and (2)) were taken from a single level in the hydrodynamic model at an elevation of 15 mm above the bed (see discussion below).

The bottom boundary condition was a pick-up function:

$$p(t) = \sum_{i=1}^{m} F_i w_i C_0 \tag{9}$$

where F_i is the fraction of mass in the ith grain size fraction with fall velocity w_i. C_0 is the near-bed reference concentration for all fractions combined calculated with Eqs. (3) and (4), taking the grain size to be D_{50}. Five grain size fractions were adopted (Table 1).

The pick-up function boundary condition allows entrainment to be totally separated from settlement, a fundamentally important distinction. In essence, particles are added to the water column very close to the bed each time step, in accordance with the entrainment condition. These particles are supplementary to any particles falling from above or mixed downward by diffusion and they immediately become available for upward diffusive or convective mixing.

The separation of entrainment and settlement allows the concentration to be larger than C_0 at the bed when sediment is depositing from previous suspension events. This is fundamental to the process of "sediment pumping" whereby the concentrations slowly grow through time in response to a group of large waves. Sediment will remain in suspension and settle naturally after the passage of these large events, irrespective of the seabed concentrations. Even though the pick-up function is a concentration gradient condition, the gradient refers to the entraining component only, not the existing sediment in the water column. An entraiment rate of zero, for example, would result in a profile that naturally settles out. Pumping up of the profile is most pronounced when the wave heights are increasing through time, and settling occurs after these waves have passed. The rate of SSC increase has been shown to be much faster than the subsequent decay (Fig. 4).

No ad hoc assumptions about the parameters are needed because nearly all the necessary parameters for a model simulation are given by the above equations. The vertical mixing length or eddy diffusivity (which are interchangeable with Eq. (7)) is obtained via model calibration, rather than imposing a prescribed value.

Two types of simulation are considered: diffusion only; and diffusion plus convection. The convection calculation uses the vertical velocities provided by the hydrodynamic model $W(x,z,t)$ to move the particles vertically a distance Δd each model time step Δt where:

$$\Delta d = W(x,z,t) \Delta t. \tag{10}$$

It should be noted that this form of vertical convection due to wave orbital motion is not the same as the "convection" by small-scale vortices that Nielsen (1992) considers.

Horizontal advection is treated by extracting velocities from the hydrodynamic model at the elevation of the particles and moving horizontally a distance $\Delta x = U(x,z,t)\Delta t$ each time step.

5. Numerical modelling results

5.1. Model validation

The validated hydrodynamic model is compared to the measured currents in Fig. 10. While the boundary conditions are formed from the measured velocities, the model actually uses sea levels as boundary conditions. Thus, a comparison between measured and predicted velocities not only confirms the capacity of the model to simulate these short waves in side-view within millimetres of the bed, but also it confirms the methods and data manipulation procedures that were applied to form the boundary conditions. While some small deviations occur on the wave peaks, the overall agreement confirms that the numerical model is predicting the measured currents at 7 mm above the bed. While not shown here, the orbital motion amplitude gain between the bed and the S4 current meter at 0.8 m elevation (Fig. 5) was also reproduced by the model.

For the sediment transport simulations, all parameters except for the vertical eddy diffusivity are pre-set or calculated by the model. While values of vertical eddy diffusivity have been estimated by regression analysis of the data (Fig. 8), we confirm the sediment model by independently obtaining the eddy diffusivity using successive trial-and-error adjustments to achieve best calibration agreement between model and measurements. We calibrate the model in this way against data from Run 1 and then verify against Run 3, without changing the model settings. For these runs, a vertically uniform and constant value of eddy diffusivity is adopted, and sediment advection is neglected.

The calibration is shown in Fig. 11, while the verification is shown in Fig. 12. The vertical eddy diffusivity that gave the best calibration results in both cases was 0.0003 $m^2\ s^{-1}$. Notably, this value lies between the two estimates of 0.00016 and 0.00032 $m^2\ s^{-1}$ obtained by a fully independent analysis of the concentration profiles (Fig. 8). The agreement between the model and the measured values at all levels (see next section) and the agreement with the independent analysis of the field data to obtain eddy diffusivities both strongly support the worth of the predictive methods adopted.

5.2. The simplest model: fall velocity plus constant and uniform eddy diffusivity in the water column

The calibrated model closely follows measured instantaneous SSC at all levels (Figs. 11 and 12). The model is generally extraordinarily close to the measurements (e.g. 165 s) at 10 and 20 mm, although some small systematic deviations appear after the primary peak around flow reversal, particularly at 10 mm.

In the instantaneous comparisons of Fig. 12, the variability or apparent scatter at short time scales in the model is actually very similar to the variability in the measurements, especially at 120 mm. This "scatter" is apparently a random contribution or "washload" which is well reproduced by the La-

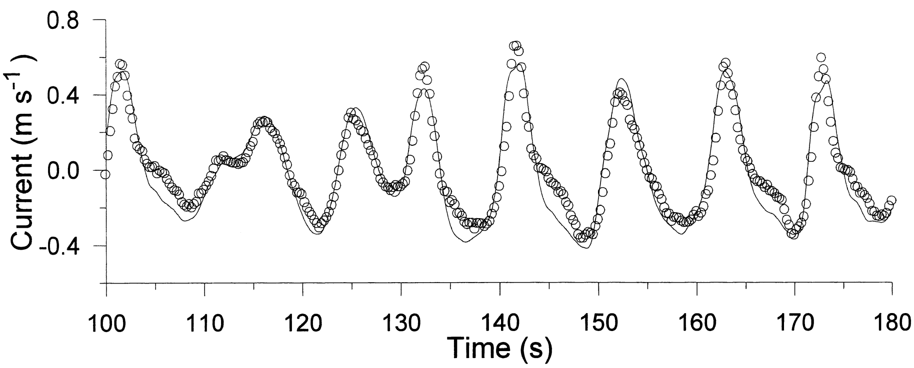

Fig. 10. The current in the HD model (solid) against the current measured by the ADV (circles).

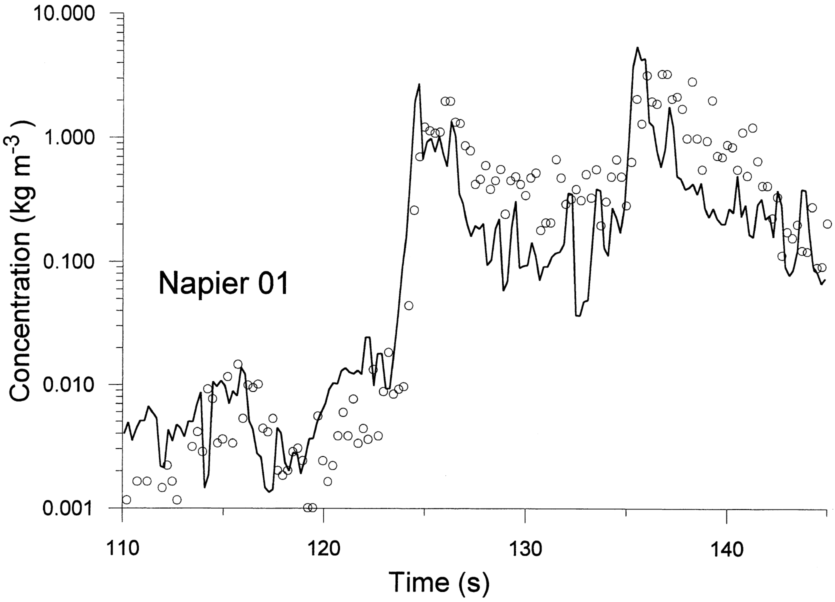

Fig. 11. Calibration of the sediment model using 40 s from Run 01. Model (solid line), field observations (open circles).

grangian model's random-walk eddy diffusivity parameterisation.

The deviations at the beginning of the simulation in the upper levels relates to the time taken for the washload to develop throughout the water column. The model follows the measured trend for accentuation of infragravity variability due to "pumping up" and decay of the upper levels during and after periods of high waves. Notably, the pumping up mechanism creating a "wash-load" of fine sediments in the upper levels is clearly shown by the predictions around 80 s at 50 and 120 mm (Fig. 12). The model starts with no sediment in suspension. A slow build-up in concentration occurs successively at each level. The upper level reaches "equilibrium" in the model after 110 s (Fig. 12), while the lower levels essentially achieve this state after the first few waves. The concentrations then vary around the average level in response to individual waves and wave groups. Thus, the pumping-up process is operating at a range of time scales from individual waves to record-duration.

In addition to the temporal comparisons, the mean (time-averaged) SSC and near-bed reference concentrations over the model simulation also show good agreement with the measurements (Fig. 13). Interestingly, the curvature of the time-averaged SSC profile is being reproduced, even though the vertical eddy diffusivity is uniform. This may be surprising because, for a uniform eddy diffusivity, a log–linear profile would be expected from the model. Inspection of the model prediction shows that the grain size reduces with elevation. As such, predicted SSC is larger in the upper levels than would be obtained in the absence of these fine constituents, and the curvature in the measured SSC profile is thereby explained. The small deviation between measurements and predictions at the upper levels results because only five grain size constituents, which do not fully represent the fine tail of the grain size population, were used in the model.

5.3. Addition of advection

Inclusion of advection of sediment by the numerically predicted vertical wave orbital currents (convection) has no significant effect on the results (compare Figs. 12 and 14). While the variability of the predictions is slightly increased, convection otherwise causes no discernable improvement. This result could have been expected from linear wave theory or

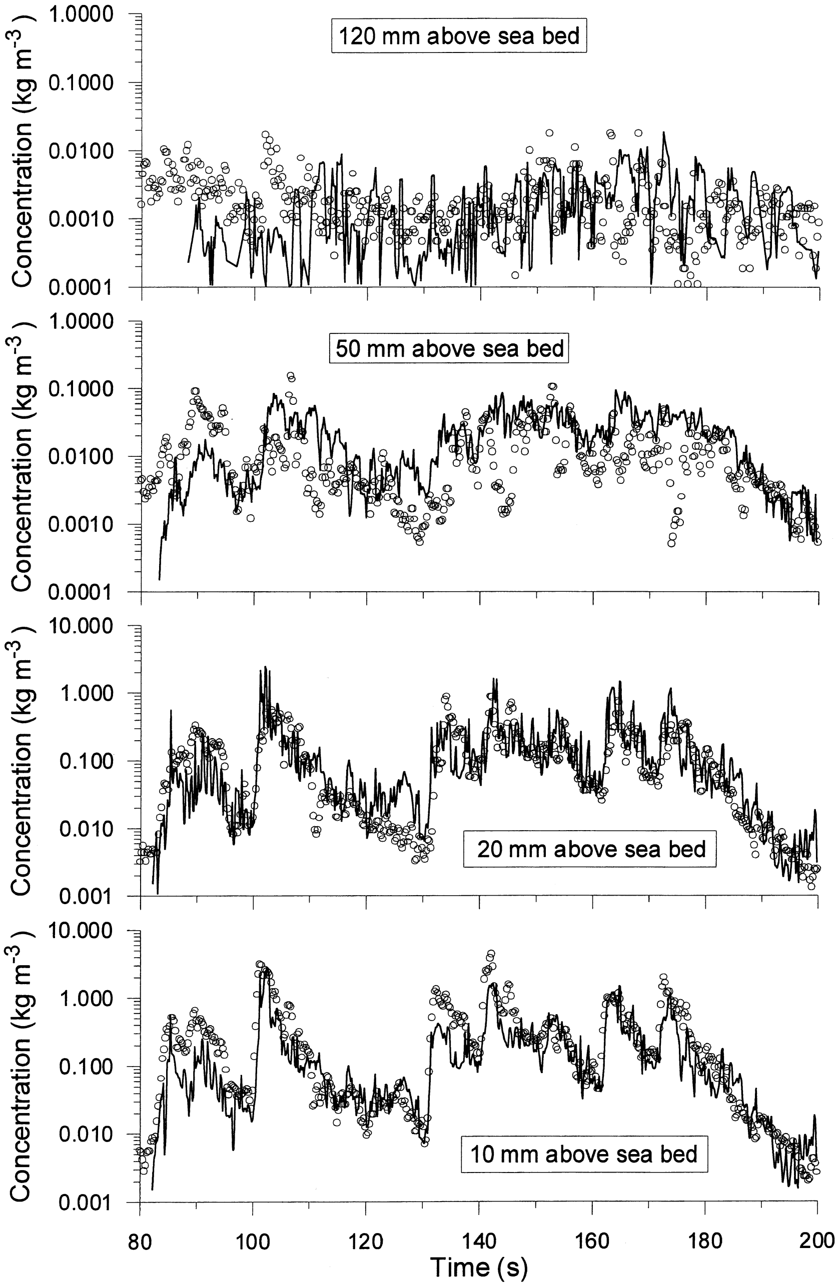

Fig. 12. Comparison of the model (solid line) with measurements at four levels, 10, 20, 50 and 120 mm (open circles) for Run 3 with diffusion only.

a one-dimensional model, but it is useful to confirm the expectation against the micro-scale measurements, particularly at flow reversal.

The change in the results is insignificant because both the measured and model-predicted vertical velocities are highly variable and relatively small near

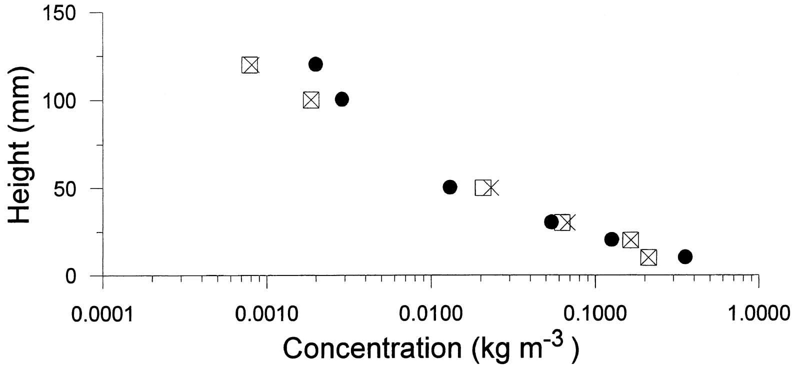

Fig. 13. Comparison of the average concentrations from the model with diffusion only (crosses), the model with diffusion and advection (squares) and for the field measurements (solid dots).

the bed (Fig. 15). Indeed, the measured and predicted velocities are mostly less than 0.01 m s^{-1} which is only half the median fall velocity of 0.02 m s^{-1}. Thus, vertical advection is normally too weak or short-lived to overcome the fall velocity of the sediment and it therefore has little effect on the SSC and cannot explain the observed suspension events around flow reversal after the wave crest.

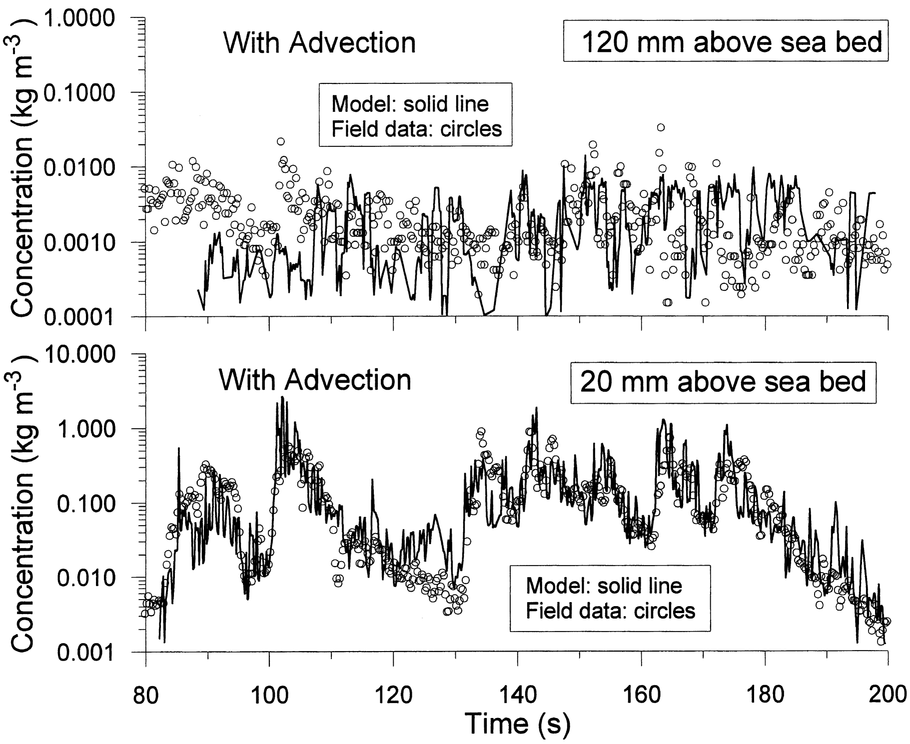

Fig. 14. Comparison of the model (solid lines) with measurements (open circles) at 20 and 120 mm, including the effects of advection.

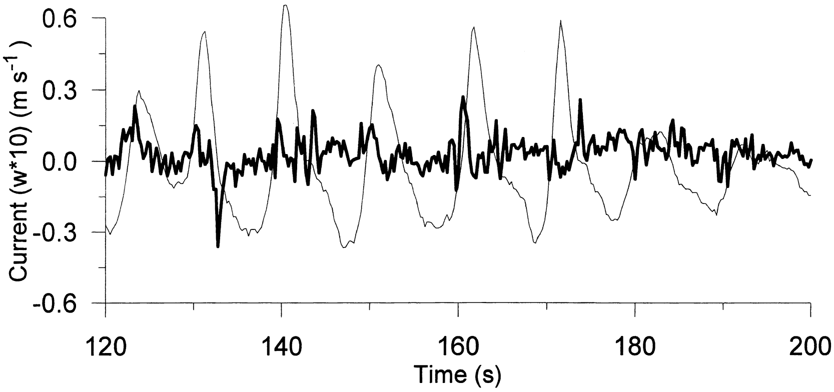

Fig. 15. The shore-normal horizontal $[u]$ (light line) and vertical $[w]$ (heavy line) current speeds from the ADV. Note the w velocity is shown at $10\times$ scale.

5.4. Suspension at flow reversal

Here, we examine the near-bed hydrodynamics using the numerical model to seek possible mechanisms for the flow reversal suspension occurring in the measured data. The presence of strong harmonics in the field measurements and the laboratory finding that suspension at flow reversal is more pronounced under asymmetric waves (Ribberink and Al-Salem, 1992) led us to compare boundary layer dynamics under symmetrical and asymmetrical waves.

5.4.1. The importance of harmonics in relation to boundary layer shear

Five numerical simulations (S1–S5) were undertaken with different harmonic amplitudes to simulate the effect of short-crestedness and the presence of harmonics which develop as the wave approaches the breakpoint (Table 2).

To consider the bed stress and the potential for generation of turbulent kinetic energy, we extracted from the model the velocity shear in the bottom 20 mm above the bed using velocities taken from the model layer closest to the bed (U_B, centred on 5 mm) and from above the wave boundary layer (U_T, centred on 25 mm). The shear is given by:

$$\text{Shear} = n\left|\frac{\partial U}{\partial z}\right| \tag{11}$$

where:

$$n = \frac{U_B U_T}{|U_B U_T|}.$$

The velocity shear is presented as positive when the velocities in the two layers have the same sign (irrespective of flow orientation) and negative when the currents are opposed. These are described here as

Table 2

Schematic wave Cases 1–5. Case 1 has no harmonics; Case 2 has harmonics with 25% amplitude reduction; Case 3 has harmonics with 50% amplitude reduction; Case 4 has a reduced third harmonic and Case 5 has no third harmonic. Amplitudes are in metres and periods in seconds

Case 1		Case 2		Case 3		Case 4		Case 5	
Amplitude	Period	Amplitude	Period	Amplitude	Period	Amplitude	Period	Amplitude	Period
0.2	10	0.16	10	0.12	10	0.20	10	0.2	10
		0.04	5	0.06	5	0.10	5	0.1	5
		0.01	2.5	0.03	2.5	0.04	2.5		
				0.015	1.25				
				0.0075	0.625				

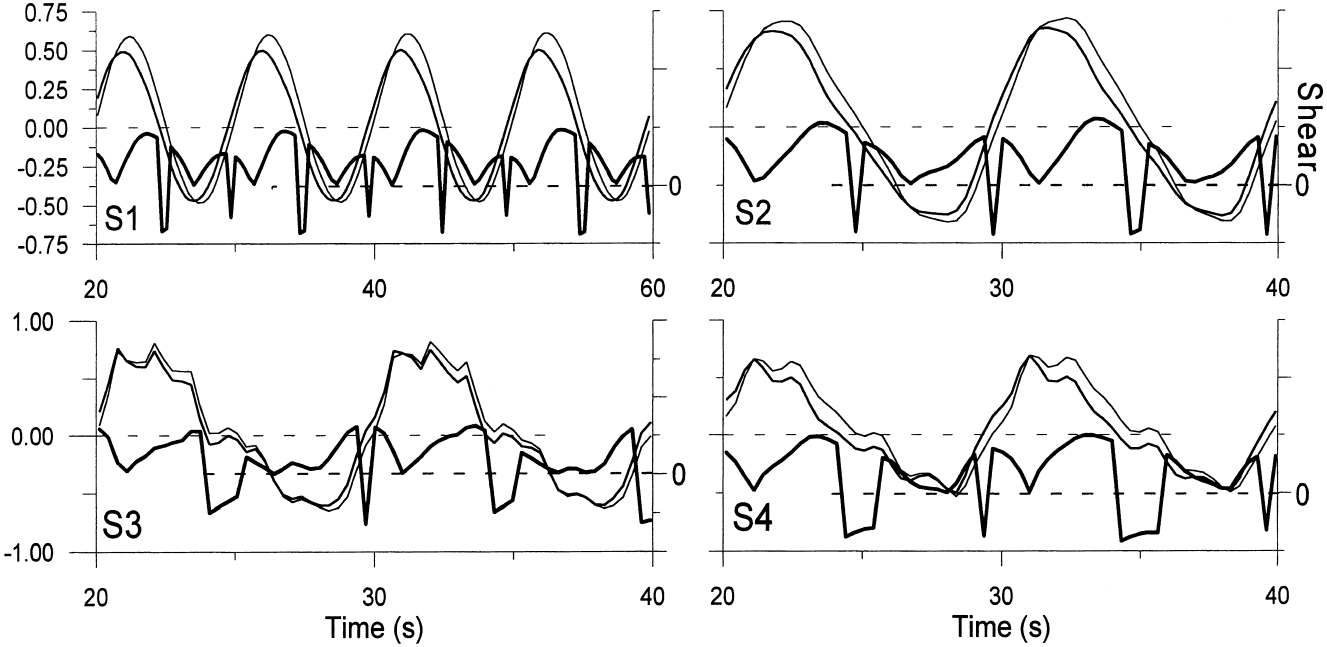

Fig. 16. Synthetic waves applied in the HD model, consisting of a summation of sine waves, with harmonics for Cases S1–S4. The shear between 0.005 and 0.025 mm above the bed is also shown (heavy line). The periods of *adverse shear* have been accentuated by plotting these as their *negative values*. See Table 2 for amplitudes of harmonics included.

"positive" and "adverse" shear. The term "adverse shear" differentiates this process from suspension associated with the wave orbital intensity.

Fig. 16 shows the currents in the two layers and the shear (Eq. (11)) for Cases S1–S4. For symmetrical waves (Case S1, Fig. 16), the near-bed shear is significantly larger during the decelerating (adverse pressure gradient) than the accelerating phase. Positive shear reaches a maximum after the crest and slowly decreases to zero in the trough. Adverse shear appears around flow reversal during flow acceleration and deceleration. However, adverse shear is larger and longer-lived during the decelerating phase. The duration of the adverse shear pulse is of order 0.5 s.

With the addition of harmonics, the wave profile begins to adopt a strong similarity to the field measurements with the harmonics being most evident after the crest. The broad "shoulder" in the flow has also developed after flow reversal. In addition, Case S4 exhibits the "twin peaks" on the crest which were observed in the SSC's (Fig. 7), while other combinations of harmonics produce three peaks (Case S3, Fig. 16). The adverse shear around flow reversal is considerably enhanced in the strongly asymmetric cases (Cases S3 and S4, Fig. 16) during flow deceleration, but is much less affected during the accelerating phase.

5.4.2. Consideration of the effect of adverse shear on SSC

Quite possibly, the adverse shear could enhance near-bed turbulence. If so, the adverse shear may provide a mechanism for the short-duration burst of entrainment around flow reversal. To test this mechanism, we include additional suspension in the model during the period of adverse shear in the decelerating phase (Fig. 17). As in Black (1994), the reference concentration during the short period of adverse shear is taken to be equal to the value that was predicted by the sediment model under the previous wave crest. However, unlike the previous study where the duration of the pulse was determined by sediment model calibration, the timing of additional suspension is obtained from the predictions of adverse shear occurrence by the numerical hydrodynamic model.

In accordance with the analysis of the field data to obtain mixing lengths and eddy diffusivities (Fig. 8), the eddy diffusivity was doubled during the period of adverse shear. The factor of 2 is based on field measurement analyses and is imposed to test the importance of the adverse shear mechanism. With this enhancement, the sediment model was recalibrated to obtain new eddy diffusivity values of 0.00025 and 0.00050 m^2 s^{-1} during positive and adverse shear. Notably, these bound the constant value of 0.0003 m^2 s^{-1} used for previous simulations.

The change to eddy diffusivity arises because of the sensitivity of SSC to this parameter. Indeed, it is the sole agent responsible for upward mixing of sediment under a gradient diffusion assumption. However, sensitivity tests with the hydrodynamic model showed that the timing of the adverse shear is unaffected by changes to the magnitude of the eddy diffusivity. Fig. 9b shows three cases of eddy diffusivity including uniform values of 0.00025 and 0.00050 m^2 s^{-1} and differences in the predicted shear only occur around peak flow when currents are

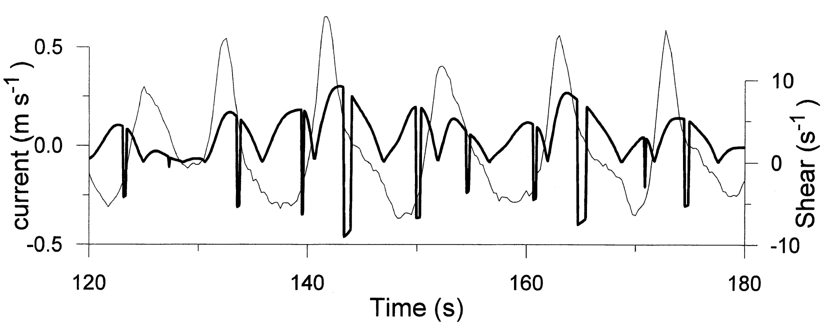

Fig. 17. Shear (adverse shear shown as negative values) from the model (heavy line) and measured currents.

strongest. However, the timing of the adverse shear pulses used by the sediment model is unaffected, and so different simulations of the hydrodynamic model were not required.

The pattern of predicted SSC with the enhanced model is subtly altered (Fig. 18). Comparing Figs. 12 and 18, the peaks at 10 mm are better predicted. A prime example is the peak at 145 s where both the

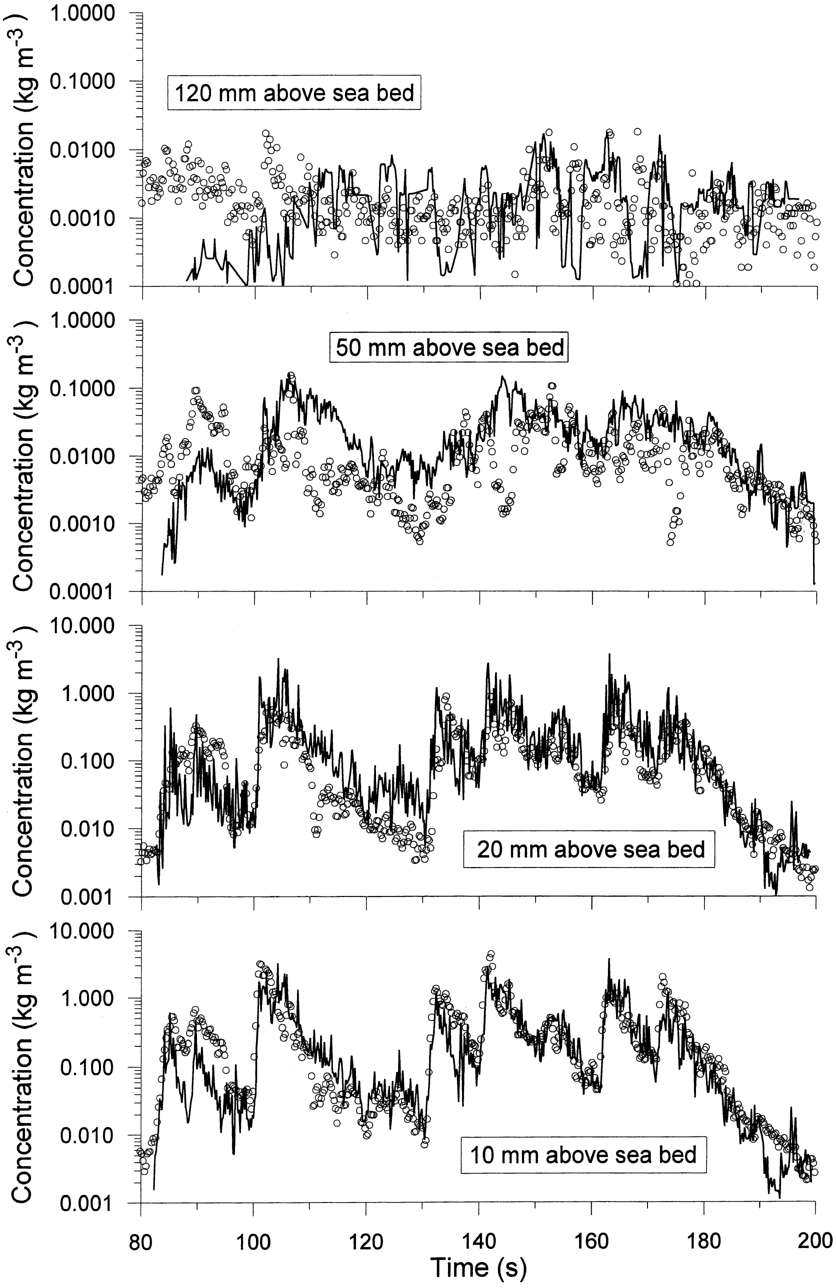

Fig. 18. The model predictions at 10, 20 and 30 mm (solid lines) with the inclusion of enhanced (doubled) diffusion during periods of adverse shear, indicated by the negative values assigned to the shear at this time. The measurements are shown as open circles.

primary and secondary peaks are present in the enhanced model predictions. The secondary peak is only a short-duration burst. At 20 mm, the secondary peaks are better predicted, although a high-frequency random component is also accentuated. At 50 mm, the model now reproduces the peak at 105 s but the decay in concentration appears to be too slow, which causes a 10-s over-estimation of concentration that affects the 20 mm level via the sediment falling out of suspension. The effect of this over-estimate is only just apparent at 10 mm where mean SSC is much larger. At 120 mm, the enhanced model appears to be more adept at predicting the highest concentrations during the high waves from 140–180 s.

6. Discussion and conclusions

The capacity of the hydrodynamic model to predict near-bed currents was confirmed and several critical factors determining SSC have been identified. First, we have shown that close prediction of instantaneous SSC over plane beds can be achieved using high-resolution hydrodynamic and sediment transport models, even under irregular asymmetric waves (Figs. 12, 13 and 18). On the contrary, instantaneous SSC could not be predicted using simple empirical relationships based on wave orbital motion alone (Fig. 6).

The hydrodynamic model showed that near-bed shear in the current varied considerably in response to the constantly accelerating and decelerating flows, particularly under asymmetric waves. Moreover, around flow reversal, predicted near-bed currents were often oppositely directed over the lowest 20 mm of the water column. The presence of velocity shear alone is not necessarily a mechanism for increased diffusion but the velocity shear is expected to be directly related to the production of turbulent kinetic energy (Savioli and Justesen, 1997). An increase in turbulence at this time is supported by measurements of higher eddy diffusivity, from the observed SSC. As in the laboratory measurements of Ribberink and Al-Salem (1992), the SSC peak associated with the wave crest was dominant up to approximately 10 mm but, above this level, the flow reversal peak was more pronounced. This is explained by intra-wave variability in vertical eddy diffusivity. Mixing lengths for the laboratory data were 4.5 and 9.4 mm under the crest and at flow reversal, respectively (Black, 1994). For the present case, the mixing lengths were similar and equal to 8 and 16 mm. In both cases, the mixing length increased by a factor of 2 from the wave crest to flow reversal. Using a k–ε model, Savioli and Justesen (1997) have been able to reproduce this short-duration increase in eddy diffusivity around the time of flow reversal, as indicated by the sediment modelling of Black (1994).

The numerical model demonstrated that the magnitude and duration of the adverse shear was dependent on the size of the wave harmonics responsible for wave asymmetry. Under non-linear shoaling waves, the harmonics are phase locked to the wave peak and so they cause similar distortions in the profile of successive waves, including a distortion around flow reversal. Under highly asymmetric waves, the duration of the adverse shear was approximately 1 s for a wave with 10-s period, while under symmetrical waves, the adverse shear was shorter lived (about 0.3 s).

The presence of a pulse of strong (adverse) shear could explain: (1) the observation that flow reversal entrainment becomes more pronounced under asymmetric waves; and (2) the tendency for entrainment after the wave crest, rather than on the leading face of the wave. The similarity between the “twin peaks” in observed SSC and in the shear from the idealised asymmetric wave profiles (Fig. 16) may also explain these multiple suspension peaks observed after peak flow.

In all cases, the adverse shear is longer lived and more intense during flow deceleration than flow acceleration (Fig. 16). Higher shear during deceleration is evidenced by higher eddy diffusivity at this time, depicted by the closer SSC isolines in Fig. 7 after peak flow. The fact that near-bed shear was predicted to be largest during the decelerating phase (Fig. 16) may similarly explain why SSC was larger during the decelerating phase than the accelerating phase, for the same orbital current magnitude (Figs. 6 and 17).

While flow reversal entrainment is occurring, we have also demonstrated that measured SSC can be quite well predicted without such entrainment and using constant, uniform eddy diffusivity in the water column. Convection associated with predicted wave orbital currents had no discernable influence. Moreover, the measured vertical currents were mostly small and typically, only half the median fall velocity. Some care needs to be taken with the definition of currents responsible for convection. Strictly, Nielsen (1992) considers small coherent vortices and these may be generated by near-bed shear associated with bed roughness, rather than vertical wave orbital motion. We have modelled coherent orbital velocities but have measured all vertical components at 4 Hz. In both instances, the near-bed currents were small and apparently not the primary process responsible for the measured SSC.

Fig. 17 shows the predicted shear stress from the hydrodynamic model which could have been used in the sediment model to obtain the Shields stress for prediction of entrainment. While this was not done here, Fig. 17 interestingly shows that the maximum in shear stress lags the wave orbital velocity peak, while the predicted shear from the Shields Eq. (4) always remains in phase with the orbital motion. Notably, careful inspection of Fig. 18 indicates that the timing of the sharp increases in SSC at 10 mm on the steep faces around peak flow is very close to the measurements. Indeed, had the shear prediction of the numerical hydrodynamic model been used for the entrainment, rather than Eq. (4), the prediction of suspension would have lagged by up to 2 s and a much poorer prediction would have been obtained.

The use of a gradient diffusion technique with uniform diffusivity is justified by the time series predictions of SSC, but is further strongly supported by the measured time-averaged concentration profile that exhibited upward concave behaviour (Fig. 13). It has been pointed out by Nielsen (1992) that SSC profiles change from upward convex for small wT to being upward concave for large wT with a range in the middle where profiles are exponential. This has been observed with uniform sand in the laboratory for both rippled and sand beds. The fact that we have predicted the observed upward concave profile for a population of grain sizes with uniform diffusivity and an irregular wave pattern is a weighty argument for the gradient diffusion assumption. Moreover, the result suggests that concave-upward profiles are not necessarily an indication of changing mixing length or eddy diffusivity with elevation, as the diffusivity was vertically uniform in the model.

There are several precedents in various environments, including rippled beds, for the methodologies adopted to predict the SSC (Black, 1994; Green and Black, 1998). The important commonalities are: (1) the uniform vertical eddy diffusivity which could vary through the wave cycle; (2) a pick-up function with empirical coefficients given by Eq. (3); (3) the Lagrangian techniques which separate entrainment and settlement; and (4) the random walk diffusion. Over rippled beds, the empirical constant 0.005 in Eq. (3) was found to increase to 0.1 (Black et al., 1997; Green and Black, 1998), in accordance with the correction for flow contraction recommended by Nielsen (1986).

Unresolved key issues are why the entrainment magnitude at flow reversal, given by the near-bed reference concentration, should be similar to C_0 from the previous wave crest and, more basically, why suspension occurs at all when the orbital currents are close to zero at flow reversal. The phenomenon of flow reversal entrainment is anomalous because entrainment has been traditionally associated with shear stress and tractive force acting directly on the sediment grains (e.g. Shields, 1936). The fluid friction velocity or shear stress is a water column outcome of the bed frictional resistance which, in turn, is said to relate to the force of the flow on the grains themselves through skin friction and form drag (e.g. Bagnold, 1954). Indeed, the results in this paper show that the timing of suspension under the wave crest is in phase with the wave orbital velocity rather than the peak in near-bed shear, although the shear stress is high at flow reversal.

Some insight is provided by the techniques applied in the numerical model in which entrainment is simulated by simply making new grains available for suspension with a concentration governed by C_0. Essentially, we need to understand the difference between a grain resting on the bed and one at the same elevation which has become "available" for suspension. One inescapable fact is that the grains cannot be suspended if the eddy diffusivity goes to zero at the bed. There must be finite diffusion or bursting-type convection at the bed (e.g. Heathershaw, 1979) for the available grains to be mixed upward, otherwise they simply fall back to the bed or never entrain at all.

We have assumed that the eddy diffusivity remains uniform all the way to the bed, even though theoretically the eddy sizes should diminish as the bed is approached. Laboratory eddy diffusivity profiles near the bed also often show a rapid rise from zero to a peak just above bed level and then a decrease to the top of the wave boundary layer (e.g. Kos'yan, 1985, his Fig. 1). Such measurements have led to a predominance of similar vertical diffusivity profiles in semi-empirical formulae for sediment suspension. Similarly, turbulent kinetic energy would be expected to increase significantly very close to the bed (e.g. Savioli and Justesen, 1997). Our results nevertheless strongly support the use of a uniform diffusivity and our concentration profile measurements were log–linear within 30 mm of the bed (Fig. 3). Possibly, the high grain concentrations, fluidisation between the grains making the "bed level" less discernable, micro-scale irregularities over natural sea beds, and wave randomness disrupt the classic diffusivity profiles, creating a more evenly mixed region of uniform diffusivity near the bed in natural environments.

Future work needs to be directed towards the specification of a near-bed reference concentration formula which does not rely on instantaneous orbital current alone for a given grain size. Increased fluidization may act to make the grains "available" for suspension. In this case, the significant difference between an immobile bed and the carpet of mobile grains under the wave crest is the level of fluidization.

The fact that the grains are moving horizontally would seemingly have no direct influence on their ultimate suspension, if grain–grain interactions are neglected. The grain interactions have been implicated in suspension by suggesting that the grains are "bumped" upwards into a new zone where diffusion takes over, or the grains are supported by their interactions in the sheet flow layer (Fredsoe and Deigaard, 1992). However, we have not distinguished any vertical zonal structure of any significance in the model. Furthermore, the concentration profile measured with the ABS was essentially log–linear to within 5 mm of the bed (Fig. 3) and we have successfully simulated the SSC with a uniform eddy diffusivity and no special treatment of the sheet flow layer.

If fluidization in the presence of turbulence is a distinguishing characteristic that allows suspension to proceed, then, at flow reversal after the crest, the downward vertical velocities in conjunction with the measured higher turbulence may penetrate the already highly mobile and loosely packed surface grains and could thereby enhance the sediment suspension at that time. It may be that bursting events simultaneously entrain the grains and cause the eddy diffusivity to rise around flow reversal. The bursting may explain the entrainment, while the increased diffusivity explains the observed concentrations within the water column.

While the suggestion that adverse shear is more effective at producing turbulence than positive shear is intuitive, this cannot be assumed. Indeed, the adverse shear magnitudes are approximately equal to the positive shear (Figs. 16 and 17). Moreover, most entrainment occurs at flow reversal after the wave crest when the flow near the bed is predicted to be downward and entrainment by fluidization (or bursting) may be implicated. With our success in predicting the intra-wave suspension at high resolution, future research needs to be directed at the fundamental processes in the bottom few millimetres where entrainment initiates (e.g. Flores and Sleath, 1998). However, broader laboratory data may be needed because measurements such as those of Flores and Sleath (1998) do not appear to show the sediment entrainment at flow reversal or the multiple peaks after the crest, as identified in the field measurements presented here.

Acknowledgements

We thank the NZ Foundation for Research, Science and Technology in the programme "Wave and Sediment Dynamics in Coastal and Estuarine Systems" (Grant C01618). In addition to the support of this project by NERC under the Small Grants programme, CEV would like to acknowledge the NIWA Visiting Scientists Programme (Grant VSK802). Both CEV and KPB wish to thank colleagues and staff at NIWA and students from the University of Waikato for their assistance with this project.

References

Bagnold, R.A., 1954. Experiments on a gravity-free dispersion of large solid spheres in a Newtonian fluid under shear. Proc. R. Soc. London, Ser. A 225, 49–63.

Black, K.P., 1994. Suspended sediment load during an asymmetric wave cycle over a plane bed. Coastal Eng. 23, 95–114.

Black, K.P., 1995. The numerical hydrodynamic model 3DD and support software. Occasional Report No. 19. Department of Earth Sciences, University of Waikato, New Zealand, 53 pp.

Black, K.P., Rosenberg, M.A., 1991. Suspended load at three time scales. Coastal Sediments '91. Waterway, Port. Coastal Ocean Div. (ASCE) 1, 313–327.

Black, K.P., Gorman, R.M., Symonds, G., 1995. Sediment transport near the break point associated with cross-shore gradients in vertical eddy diffusivity. Coastal Eng. 26, 153–175.

Black, K.P., Osborne, P.D., Green, M.O., Villard, P.V., 1997. Intra-wave suspended sediment concentrations over bedforms. Pacific Coasts and Ports '97 Conference, Christchurch, 7–11 September.

Davies, A.G., Li, Z., 1997. Modelling sediment transport beneath regular symmetrical waves and asymmetrical waves above a plane bed. Cont. Shelf Res. 17 (5), 555–582.

Flores, N.Z., Sleath, J.F.A., 1998. Mobile layer in oscillatory flow. J. Geophys. Res. 103, 12783–12793.

Fredsoe, J., Deigaard, R., 1992. Mechanics of Coastal Sediment Transport. World Scientific Publishing, Singapore, 369 pp.

Green, M.O., Black, K.P., 1998. Suspended-sediment reference concentration under waves: field observations and critical analysis of two predictive models. Mar. Geol. (in press).

Heathershaw, A.D., 1979. The turbulent structure of the bottom boundary layer in a tidal current. Geophys. J. R. Astron. Soc. 58, 395–430.

Kos'yan, R.D., 1985. Vertical distribution of suspended sediment concentrations seawards of the breaking zone. Coastal Eng. 9, 171–187.

Murray, P.B., Soulsby, R.L., Davies, A.G., 1991. Sediment pick-up in wave and current flows. In: Soulsby, R.L., Bettess, R. (Eds.), Proceeedings of EUROMECH 262 Colloquium on Sand Transport in Rivers, Estuaries and the Sea, vol. 1. A.A. Balkema, Rotterdam, pp. 37–43.

Murray, P.B., Soulsby, R.L., Davies, A.G., 1993. Sediment pick-up in combined wave current flow: Data Report. Report SR364, Hydraulics Research, Wallingford, 72 pp.

Nielsen, P., 1986. Suspended sediment concentrations under waves. Coastal Eng. 10, 1–21.

Nielsen, P., 1992. Combined convection diffusion modelling of sediment suspension under waves. Proc. 23rd International Conference on Coastal Engineering, Venice. ASCE. pp. 3202–3215.

Osborne, P.D., Black, K., Villard, P.V., Douglass, S., 1997. Field measurements of 3-D velocity structure and suspended sediments under locally generated waves and swell. Pacific Coasts and Ports '97 Conference, Christchurch, 7–11 September. .

Ribberink, J.S., Al-Salem, A.A., 1992. Time-dependent sediment transport phenomena in oscillatory boundary-layer flow under sheet flow conditions. Delft Hydraulics Data Report H840.20, Part VI, Delft.

Savioli, J., Justesen, P., 1997. Sediment in oscillatory flows over a plane bed. J. Hydraul. Res. 35 (N2), IAHR.

Shields, A., 1936. Awendung der Ahnlichkeits Mechanik und der Turbulenzforschung auf die Geschiebe Bewegung., Preuss. Versuchanstalt fur Wasserbau und Schiffbau, Berlin.

Swart, D.H., 1974. Offshore sediment transport and equilibrium beach profiles. Pub. No. 131., Delft Hydr. Lab.

Vincent, C.E., Downing, A.J., 1994. Variability of suspended sand concentrations, transport and eddy diffusivity under non-breaking waves on the shoreface. Cont. Shelf Res. 14, 223–250.

Vincent, C.E., Osborne, P.D., 1995. Predicting suspended sand concentration profiles on a macro-tidal beach. Cont. Shelf Res. 15 (13), 1497–1514.